RSC Advances

ROYAL SOCIETY
OF CHEMISTRY

www.rsc.org/advances

Origin of blue emission in ThO_2 Nanorods: Exploring it as a host for photoluminescence of Eu^{3+}, Tb^{3+} and Dy^{3+}

Santosh K. Gupta[a]*, P.S. Ghosh[b], A. Arya[b], V. Natarajan[a]

a. Radiochemistry Division, Bhabha Atomic Research Centre

b. Materials Science Division, Bhabha Atomic Research Centre

Trombay, Mumbai-400085, India

*Corresponding Author- santufrnd@gmail.com

Telephone- +91-22-25590636

Fax- +91-22-25505151

Abstract:

Nanorods of ThO_2 were synthesized in a reverse micelle using Cetyl trimethyl ammonium bromide as a surfactant and characterized by X-ray diffraction and transmission electron microscopy. Europium, terbium and dysprosium was doped at 1.0 mol% level and was confirmed using XRD. A Photoluminesence study shows that nanorods of thoria emit blue color on UV-excitation. Lifetime and electron paramagnetic resonance (EPR) spectroscopy shows blue emission is because of oxygen vacancy. First principles calculations using projector augmented wave potentials and generalized gradient approximations predicts the structural relaxations due to neutral and positively charged oxygen defects in bulk thoria leads to symmetric distortion around the vacancy site and this prediction is complemented by experimentally measured highly symmetric isotropic signal with g = 1.959 in EPR studies. Density of states analysis shows presence of defects states mainly contributed by Th d and f states near the conduction band minima for the double positively charged oxygen vacancy and radiative transitions from these states qualitatively explains blue emission in thoria. Based on the time resolved emission data (TRES), it has been inferred that, two different types of Ln^{3+} ions were present in the thoria nanorods. A long lived species (τ~1.5 ms) was present at cubic site with O_h symmetry and the other was a short lived species (τ~ 300 μs) present at the non-cubic site with C_{3v} symmetry. Most of Eu and Tb are distributed in cubic site with O_h symmetry whereas Dy is mainly localized at the non-cubic site with C_{3v} symmetry. Under UV light excitation, $ThO_2:Ln^{3+}$ nanorods show the characteristic f–f transitions of Ln^{3+} (Eu, Tb and Dy) ions and give bright red, green, bluish -yellow emission, respectively. In addition, multicoloured luminescence containing white emission has been successfully achieved for tri-doped $ThO_2:Ln^{3+}$ phosphors by simultaneously doping all three lanthanides ions and adjusting their doping concentrations due to the simultaneous luminescence of Ln^{3+} in the ThO_2 host.

1. Introduction:

Solid state light emitting diodes are widely used nowadays in various applications such as small signal lights, indicators and signs, house lighting, street lighting and many others. Depending on a bang gap of the material LEDs can emit in a wide wavelength range: from UV to IR. In the context of global energy shortage, energy-saving is an important issue that we are facing on. In the field of lighting, white light emitting diodes (LEDs), a new generation solid source have been a highlight due to high luminous efficiency, low energy consumption and great potential in environmental protection. Thereafter there is a present trend to replace the traditional incandescent and fluorescent lamps [1, 2]. Nanoscale phosphors may have a number of potential advantages over traditional micron-sized phosphors. They have somewhat different electrical, optical, and structural characteristics which are caused by quantum effects due to their high surface to volume ratio. This increases the band gap by reduction of the number of allowable quantum states in the small particles and improves surface and interfacial effects [3, 4]. In addition, quantum confinement in nanocrystalline materials may result in an enhancement of their luminescence [5]. It is important to control the size and size distribution of the nanoparticles during the synthesis. The properties of nanoparticles strongly depend on the size and therefore monodisperse nanoparticle solutions are necessary to study the size-dependent properties. Monodisperse nanoparticle solutions are also necessary to control the organization on substrates or in 3D space [6]. Control of the size and size distribution of nanoparticles during the synthesis can be obtained by confinement in tight cavities, like zeolites, dendrimers, or reversed micelles. In reversed micelles the size of the water pools can be controlled, and with the size of the water pools the size of the nanoparticles [7].

Thorium oxide in particular is very important w.r.t nuclear industry. It is well known that thorium oxalate is a starting material for the purpose of obtaining thorium oxide, which is then to be used as a nuclear fuel in nuclear reactor since it, gives birth to ^{233}U, which is a fissile element, by neutron bombardment. Thorium oxide, ThO_2, has long been an important component in the nuclear industry [8-12] and has more recently found utility in the design of a variety of new materials, including catalysts [13-16], electrodes [17-19], fuel cell electrolytes [20] and sensors [21]. For each of these applications, one must be able to reliably control composition, porosity and densities of the thoria products.

Thorium dioxide is an interesting host matrix for a variety of reasons like its highest phonon energy is low (~ 450 cm^{-1}) [22, 23] which lowers the non-radiative losses. Also, it crystallizes in the fluorite structure with a lattice constant of 0.56 nm. The ionic radius of Th^{4+} is 0.104 nm, making the substitution of all of the rare earths possible.

The phonon energy of the host for rare-earth ions is a crucial factor to be considered for developing luminescent materials. The thorium dioxide can satisfy both low phonon energy environment for rare-earth ions and good chemical and mechanical stabilities for practical use thus the rare-earth-doped thorium dioxide are developed in this study and expected to be a kind of promising optical materials with favorable performances. Very recently, we reported Sm doped ThO_2 to generate warm white light for white LED [24]. However, to obtain the better quality of white emission, more emission bands covering a broad visible region are highly desirable. Due to the comparable ionic radius of Th^{4+} with that of lanthanide ions, ThO_2 is expected to be a good host for doping lanthanide ions. Such lanthanide ion doped ThO_2 nanomaterials are potential candidates for photonic and luminescent applications. Other advantage of using thoria as a luminescent host is it stability and as it doesn't undergo any phase transition.

Among all the chemical processes, the micro emulsion processing (reverse micelles synthesis) has been demonstrated as a very versatile and reproducible method. The reaction takes place in the aqueous cores of the reverse micelles which are dispersed in an organic solvent and are stabilized by a surfactant. The dimensions of these aqueous cores are in the nanoregime and are thus being referred to as nanoreactors. The product obtained after the reaction is homogeneous. The other advantage of using this methodology is that the morphology of the product can also be controlled as the surfactant aggregates from a variety of structures which are used as templates. The size of the core of the reverse micelles can also be controlled by changing Wo ([H2O]/ [surfactant]). Thus, the size and morphology of the product can be controlled by proper choice of the composition of the microemulsion system. Thoria as a luminescent host is relatively unexplored. We are the first group to report on warm white light emission from thoria nanorods derived using reverse micellar route [24]. The low-phonon energy thoria ($\sim$ 450 cm^{-1}) opens up the possibility of more efficient luminescence from the activator ions incorporated in it. This is due to the fact that the lower the phonon energy of the host, the higher the number and probability of radiative transitions of substituted rare earth ions. Thus, rare earth ion doped nano ThO_2 can be a good choice as phosphor materials for white light emitting UV-LEDs.

For this purpose, herein we developed Eu/Tb/Dy tri-doped thorium oxide nanorods, which are revealed as promising candidates for realization of resin-free and long-life LED devices. Reports on luminescence properties of singly doped lanthanide do exist in literature but none of them tried to exploring the possibility of using it as host for pure white light emission. Chandrasekhar *et al.* has reported on non-radiative transition probability of

lanthanides doped thoria [25]. Lin *et al. has* synthesised thoria nanotubes using sol-gel method and discusses about the symmetry of europium and optical properties of $ThO_2:Eu^{3+}$ [26]. In this context Godbole *et al.* has reported on Photo-luminescence characteristics of Pr^{3+} in ThO_2 and investigated the role of defects in a photo-induced charge transfer [27]. The same group has also reported on photo and thermoluminescence of Tb^{3+} in ThO_2 [28]. Yin et al. has reported on site symmetry and site selective spectroscopy of Eu and Dy in ThO_2 [29, 30]. But none of them exploited the behavior in nanocrystalline thoria and towards white light emission. Also none of the researcher has tried to explain the emission from nanocrystalline thoria without any activator ion. We have taken up this challenge of synthesizing radioactive nano thoria and explained the origin of visible emission using emission and EPR spectroscopy. We also calculate electronic structures of pure thoria as well as oxygen defects (neutral and charged) using first principles calculations in order to understand photoluminescence behaviour of thoria in the presence of oxygen defects. For balanced white light, a proper combination of red, green, and blue emission is desirable for better color rendering capability of the phosphor. The CIE coordinates of the balanced white light region of the chromaticity diagram lies in the range x = 0.28–0.35, y = 0.30–0.37, and a CCT value of 6,500 K (D65 point) corresponds to that of bright noon daylight. However, to the best of our knowledge, there are no reports on rare earth ions tri-doped ThO_2 nanophosphors giving balanced white light emission. In this article, we report the synthesis of nanocrystalline ThO_2: RE (RE = Eu^{3+}, Tb^{3+}, and Dy^{3+}) by reverse micellar synthesis. We have tried to explore the luminescence properties of Eu, Tb and Dy in ThO_2 in terms of their local structure and site symmetry.

2. Experimental:

2.1. Nanoparticles synthesis in reverse micelle

ThO_2 nanoparticles were synthesized by the thermal decomposition of thorium oxalate precursor using the method reported in our earlier work [24]. The precursors were synthesized by the reverse micellar route with CTAB (Cetyl trimethyl ammonium bromide as the surfactant, 1-butanol as the co-surfactant and iso-octane as the nonpolar solvent. Initially the precursor thorium oxalate is prepared. The thorium oxalate nanorods were synthesized by using a reverse micellar route. The microemulsions (A) were synthesized using 39.6420 g of CTAB, 40.4 ml of 1-butanol, and 200 ml of isooctane in a conical flask. Then 24 ml of 0.1 M thorium nitrate solution was added drop wise while stirring to obtain a colourless solution. Another microemulsion (B) was prepared using an aqueous solution of ammonium oxalate,

keeping the other constituents identical. The two microemulsions (A and B) were mixed while stirring and kept for 15 h. The solution became cloudy and a white precipitate was obtained. The product was centrifuged and washed (thrice) with a mixture of chloroform: methanol (1:1) and dried at room temperature. The oxalate product was dried overnight at 500^oC for 6 h to obtain thorium oxide. For preparation of lanthanide doped sample, appropriate quantities of Eu/Tb/Dy nitrate, were added at the initial stage, after adding thorium nitrate.

2.2. Instrumentation:

X-ray diffraction (XRD) measurements were carried out on a STOE X-ray diffractometer using a Ni filter, scintillation counter and graphite monochromator. The diffraction patterns were obtained using monochromatic Cu-Kα radiation (λ= 1.5418Å), keeping the scan rate at 1sec/step in the scattering angle range (2θ) of 10° to 60°. To obtain the crystallite size from X-ray line broadening, we applied Scherrer's formula (t=0.9λ/B cosθ), where t is the diameter of the grain, λ is the wavelength (for Cu-K_α, λ=1.5418 Å) and B= $[(B_M^{\ 2} - B_S^{\ 2})]^{1/2}$ (B_M is the full width at half maximum of the sample and B_S is that of a standard grain size of around 2 μm). The standard used was quartz and was chosen such that the sample and the standard have reflections at nearly similar 2θ values. TGA was carried out using SETARAM 92-18 TGA system on well ground samples in flowing nitrogen atmosphere at a heating rate of 10° C/ min. High-resolution transmission electron microscopy (HRTEM) of the oxalate precursor and thoria particles was performed on a JEOL modeled JEM-2100 F field emission electron microscope operating at 200 keV. The analysis of trace metallic impurities in the sample was determined by ICP-AES method using a computer controlled, high resolution, simultaneous atomic emission spectrometer (Spectro Arcos, Germany) equipped with ICP and D.C. arc as the excitation sources and a Charged Coupled Device (CCD) based detector. This technology offers the best advantage of choosing additional, interference free analytical lines for the elements under study.

2.3. Theoretical calculations:

Our total energy calculations are carried out by employing the plane-wave based pseudo potential method as implemented in Vienna ab-initio simulation package **[31-32]**. The electron and ion interactions are included using the frozen-core projected augmented wave (PAW) approach which combines the accuracy of augmented-plane-wave methods with the efficiency of the pseudo-potential approach **[33]**. The exchange and correlation effects are

described by the generalized gradient approximation (GGA) in the Perdew–Burke–Ernzerhof (PBE) form [34]. The thorium $6s^2\,7s^2\,6p^6\,6d^1\,5f^1$ and the oxygen $2s^2\,2p^4$ electrons are treated as valence electrons. The cutoff energy for the plane-wave basis set is 500 eV. A $2\times2\times1$ supercell is employed to study defect formation in ThO_2. For calculations of the unit cell (12 atoms) and $2\times2\times1$ supercell (48 atoms), the integration over the Brillouin zone is carried out on $16\times16\times16$ and $8\times8\times16$ k-point meshes generated using the Monkhorst–Pack [35] method, which are both proven to be sufficient for energy convergence of less than 0.1 meV/atom. The total energy of ThO_2 unit cell as well as supercells are optimized with respect to volume, shape and atomic positions as permitted by the space group symmetry of the crystal structure. The structural relaxations are performed for pure as well as each defect structure using the conjugate gradient algorithm until the residual forces and stress in the equilibrium geometry were of the order of 0.005 eV/Å and 0.01GPa, respectively. The final calculation of total electronic energy and density of states (DOS) were performed using the tetrahedron method with Blöchl corrections [36]. Defect formation energies are calculated using a methodology described in [37].

3.0. Results and discussion:

3.1 Phase purity and structure:

The as-prepared samples obtained after reverse micellar synthesis were characterized by powder-X-ray diffraction (PXRD). The XRD pattern for undoped ThO_2 matches well with the reported pattern for ThO_2 (JCPDS No- 780685) and it possesses cubic geometry (SG: Fm3m). The patterns indicates that the sample is well crystallized and the lattice parameters were calculated to be a 5.597 Å, which are in good agreement with that reported in the literature for bulk ThO_2. The XRD patterns for doped ThO_2: RE^{3+} (Eu^{3+}, Tb^{3+}, Dy^{3+}) are similar to undoped ThO_2 thus showing that the parent structure is retained in the doped samples as well. The diffraction peaks in the XRD pattern are broadened due to smaller crystallite size which was estimated using Scherrer's equation. The strongest peak (1 1 1), was used to calculate the average crystallite size (D) of the samples which was found to be ~15 nm for all the samples. The XRD patterns for undoped ThO_2 and representative doped thoria nanoparticles are shown in Fig. 1.

If the crystallites are not spherical, then Scherrer formula would give different values depending on the diffraction pattern you use to determine the size because the FWHM of a

peak (hkl) is related to the number of diffracting planes along the direction normal to the (hkl) plane (i.e. the size of the crystallite along that direction).

A particle may consist of an agglomeration of several crystallites. Therefore it is always greater than crystallite size. A crystallite in true sense is a single crystal. In a particle these crystallites are arranged in a random fashion in the sense of different lattice panes. This agglomeration of randomly oriented crystallites is called the particle or grain. As already known that XRD see the lattice planes. Therefore one can get information of crystallite size. However it can be inaccurate as it doesn't consider size distribution and shape factor.

3.2. Morphology: Electron microscopy

Representative TEM and HRTEM image of undoped ThO_2 is shown in Figure 2. The image consists of rods having length around 2-2.5μm and diameter less than 20 nm. HRTEM studies of the fluorite phases obtained at 500^oC show the crystalline nature of the nanorods, as shown by the regular lattice fringes. The selected area electron diffraction pattern (SAED) of thoria nanorods (Figure 2c) confirms the cubic structure and the sharp spots indicate the crystallinity of the particles.

3.3. Host Emission: Photoluminescence spectroscopy

The PL spectrum of as-prepared ThO_2 nanorods with the excitation wavelength of 248 nm is shown in Fig. 3. The excitation energy (248 nm/4.99 eV) used is higher than the band-gap energy, so it is easy for an electron in the valence band to be directly excited to the conduction band; moreover, it is likely to be excited to the localised levels within the forbidden gap. The PL spectra exhibit a broad blue emission band centered on ~445 nm, which is attributed to radiative recombination involving defect sites at surface of ThO_2 nano rods.

It was reported that in metal oxide nanoparticles; UV luminescence is attributed to strong near-band edge (NBE) emission due to the free-exciton recombination in each films and visible light emission by transitions of excited optical centres in the deep levels (DL) [38]. The deep level emission is usually due to the presence of oxygen vacancies located near the surface of nanorods as explained by other authors in case of oxide nanostructures [39-40]. To probe the nature of defect electron paramagnetic resonance and luminescence decay measurements were carried out on thoria nanorods.

To confirm that the emission is indeed due to oxygen vacancies; the sample is heated in both oxidizing and reducing atmosphere. Considering that treatment under H_2/Ar is

expected to favour oxygen release from thorium oxide and that they enhance the relative weight of the blue band, it can thus be concluded that oxygen vacancies are involved in the blue PL emission.

3.4. Probing the type of defects: Luminescence decay and EPR

The decay curves for ThO_2 nanorods is shown in Fig. 4 at excitation wavelength of 375 nm monitoring emission at 445 nm on a 50 µs scale using a pulsed diode laser and fitted using the bi-exponential decay equation.

$$I(t) = A_1 \exp(-t/\tau_1) + A_2 \exp(-t/\tau_2) \tag{1}$$

where τ_1 and τ_2 represent the fast and slow decay components of lifetime. A_1 and A_2 are constants which determine the contributions of the fast and slow decay component.

The decay time obtained on biexponential fitting with χ^2 value of 1.213 is 7.2 µs (82 %) and 12.4 µs (18 %). Average lifetime is 8.72 µs which is typical of defect related emission.

A unique EPR signal at g = 1.959 was observed for blank thorium dioxide sample. This is typical of charged oxygen vacancy related defects **[41, 43]**. The signal shown in EPR spectra confirms the symmetric and isotropic nature of defect.

3.5. Purity of thorium oxide nanorods: ICP AES

High Purity Thorium 1 mg /ml was analyse for its trace impurities using High Resolution Sequential Inductively Coupled Plasma-Atomic Emission spectrometry (ICP-AES) to confirm that emission in thoria nanorods is defect mediated and not because of any impurity present in it. About 200 mg of as prepared thoria nanorods sample was dissolved in a mixture of HF (0.05M) – conc. HNO_3 and heated under I.R lamp. The dissolved aliquot of supernatant solution from this mixture was leached out into a separate beaker. The residual sample was repeatedly treated with HF-HNO_3 acid mixture till the time there was no residual sample left out. Simultaneously, the leachant solution containing the dissolved sample was repeatedly heated under I.R lamp after addition of conc. HNO_3 to obtain a clear nitrate solution free from any traces of HF which may cause interference during the analysis stage. The nitrate mixture thus obtained was finally made into a known volume by addition of dilute HNO_3 (0.5M) and analyzed by ICP-AES method.

A two-point calibration for each of the analyte element was carried out using 0.5M HNO_3 and 10 ppm of multi-element standard solution which served as the lower and the higher standards respectively. Prior to the calibration of standards, the detector calibration was also carried out using 100 ppm of the multi-element standard solution so as to have a

peak search and identify the most suitable peak for each analyte. Using this method, the transition metal and lanthanides were determined. The estimates for almost all the elements was found to be in the range 1-10 ppm with a precision of ±2% RSD as can be seen from table 1 which confirmed a near total purity of the sample with respect to the above impurities.

3.6. Theoretical calculations:

Before we discuss the results of oxygen defects, we briefly address the electronic structure of bulk ThO_2. Pure thoria has a Fm-3m space group and was calculated to have equilibrium lattice parameter (a_0) of 5.619 Å, which is consistent with previous PAW-PBE calculated results of a_0 = 5.619 Å [37]. Our calculated a_0 also is in accordance with the experimentally determined a_0 = 5.598(4) Å [44]. Moreover, in thoria unit-cell each O atom has 4 nearest-neighbour (NN) Th atoms at a distance of 2.43 Å and distance between Th atoms is 3.97 Å. We also calculate total and orbital-resolved partial densities of states (PDOS) for Th and O atoms in a unit cell are also presented in Fig. 6 (a). The highest occupied valence bands (VB) located just below the Fermi level are mainly contributed by O 2p states with a little Th 6d and 5f states and have a band width of 4.25 eV. This illustrates a significant charge transfer from Th 6d and 5f states to O 2p states. In addition, the covalency of ThO_2 comes from the mixing of Th 5f; 6d, and p states into the O 2p valence bands. As for the conduction bands (CB), the DOS is mainly featured by Th 5f states, mixed with a little Th 6d and O 2p states and has a width of 1.68 eV. The PAW-PBE calculated band gap (E_g) = 4.1 eV matching well with previous PAW-GGA calculated result of 4.1 eV [37]. The underestimation of band gap compared with experimental value of 5.75 eV [45] is due to the drawback of the exchange-correlation approximation (GGA). Nevertheless the present calculations properly reproduce the DOS features as well as good insulating character of thoria.

The equilibrium lattice parameter of the supercell with one neutral O vacancy calculated after full relaxations of the supercell (volume, shape and atomic positions) is 5.62 Å which is slightly larger than defect free thoria. Structural rearrangements are restricted to the atoms immediately surrounding the vacancy site, as only Th atoms NN to the neutral V_O site move radially from the vacancy site. The Th-Th distance in this case is 4.02 Å, which is larger than the Th-Th distances away from the defect site (3.97 Å). A summary of the distances between the Th atoms around an oxygen vacancy at a different charge state is given in Table 2 for comparison. The removal of an O atom (neutral) creates a defect energy level within the band gap, ~3.75 eV above the VB (see Figure 6 (b)). Figure 6 also shows the DOS

of the system around the Fermi level and, in the inset, an enlarged view of the defect states. The defect states are solely contributed by the d and f states of the Th atoms surrounding the defect site. The Fermi-energy is present just above the defect states. The DOS features in the VB and CB region are very similar to the pure thoria.

Removing one electron from the neutral V_O leads to the V_O^+ defect. The DOS features of V_O^+ defect are very similar to the V_O defect except location of the defect states. For V_O^+ defect, the defect states are present ~3.0 eV above the VB (see Figure 6 (c)). The geometry relaxations are significantly different to the neutral case. The calculated a_0 is 5.599 Å and Th-Th distance is 4.11 Å, which is smaller for a_0 and larger for Th-Th NN distance at defect site compared to pure thoria, respectively. Removal of the electron from V_O^+ (formation of V_O^{2+} site) results in no defect states in the band gap but in new states at the bottom of the CB and the defect states are present ~3.0 eV above the VB (see Figure 6 (d)). In this case Th f states contribute slightly more than d states in the defect states. The Th atoms around the vacancy move significantly away from the vacancy site: Th atoms move ~ 0.24 Å away and Th-Th NN distance (at the defect site) is 4.21 Å.

Moreover, all the Th-Th distances at the vacancy site are equal for all types of defects which signify that the structural relaxation leads to symmetric distortion around the vacancy site. This observation from our DFT calculations is in agreement with our experimentally measured highly symmetric isotropic signal with g = 1.959 in EPR studies. We have also calculated vacancy formation energies for these defects and found a very similar trend as previously reported by Y. Lu *et al.* [37]. The calculated energy of formation values indicate that formation of V_O^{2+} is favoured near the valence band, indicating that oxygen vacancies have a tendency to donate electrons. When the Fermi level is increases to around 2.5 eV, the V_O^+ becomes energetically favourable. With further increasing the Fermi level, the neutral charge state is most probable for O vacancies, and tendency of O vacancy to donate electrons diminishes. These analyses qualitatively indicate formation of V_O^{2+} vacancy is most probable and presence of defect states near the bottom of CB enables the photo excited electrons to occupy those states and upon radiative recombination these photo electrons can produce PL spectrum in the blue region.

4. Photoluminesence spectroscopy of doped thoria nanorods

4. 1. Lanthanide ion doped ThO$_2$ (Eu, Tb and Dy)

Figure 7a shows the excitation spectra (λ_{em} = 592 nm) of Eu doped thorium oxide sample. A broadband in the region of 220–280 nm peaking at around 256 nm has been

attributed to the $O^{2-} \rightarrow Eu^{3+}$ charge transfer band (CTB), which is caused by the electron transfer from 2p orbits of O^{2-} ions to 4f shells of Eu^{3+} ions. The sharp lines in 300-500 nm are attributed to intra-configurational 4f-4f transition of Eu^{3+} in host lattice. The peaks observed at 320, 360, 380, 395, 420, 460, 480 and 500 nm were assigned to electronic transitions of $^7F_0$ $\rightarrow$ $^5H_3$, $^5L_9$, $^5L_7$, $^5L_6$, $^5D_4$, $^5D_3$, $^5D_2$ and $^5D_1$ respectively.

In ThO_2, Th^{4+} ions occupy a site of O_h symmetry. Replacing tetravalent ions by trivalent ions will require positive charge compensation to maintain the electrical neutrality. The compensation can be achieved at some distance by Th^{4+} interstitial ions. Then several centers are expected in this matrix. Apparently, the doping concentration has a very important role in determining the site symmetry **[46]**. Linares **[46]** studied this aspect and came to the conclusion that the cubic sites O_h would be predominated at low rare-earth concentration and the trigonal C_{3v} at high concentration.

Upon excitation at charge transfer band, the emission spectrum exclusively contains very weak lines of $^5D_2 \rightarrow ^7F_0$ (465 nm), $^5D_2 \rightarrow ^7F_2$ (490 nm), $^5D_2 \rightarrow ^7F_3$ (510 nm), $^5D_1 \rightarrow ^7F_1$ (535 nm), and $^5D_1 \rightarrow ^7F_2$ (555 nm) and the relatively strong bands of $^5D_0 \rightarrow ^7F_0$ (579 nm), $^5D_0 \rightarrow ^7F_1$ (592 nm), $^5D_0 \rightarrow ^7F_2$ (614 nm), $^5D_0 \rightarrow ^7F_3$ (653 nm) and $^5D_0 \rightarrow ^7F_4$ (704 nm). $^5D_{1, 2, 3} \rightarrow ^7F_J$ lines usually appear in a compound with low-lattice phonon energy, which leads to multiphonon relaxation. They are usually difficult to occur among the levels of Eu^{3+}. As shown in Fig. 7b, the emission spectra of $ThO_2:Eu^{3+}$ nanoparticles consist of emissions from the higher energy levels ($^5D_1$ and $^5D_2$) also. The presence of emission lines from higher excited states of Eu^{3+} is attributed to the low vibration energy of Th-O groups. Multiphonon relaxation by thoria is not able to bridge the gaps between the higher energy levels and the $^5D_0$ level of Eu^{3+} completely, resulting in weak emissions from these levels. We have observed such emission lines of europium in Sr_2CeO_4 **[47]**.

The orange emission at 592 nm belongs to the magnetic dipole $^5D_0$-$^7F_1$ transitions of Eu^{3+}, and the transition hardly varies with the crystal field strength. The red emission at about 615 nm ascribes to the electric dipole $^5D_0$-$^7F_2$ transitions of Eu^{3+}, which is very sensitive to the local environment around the Eu^{3+} and depends on the symmetry of the crystal field. The intensity ratio of $^5D_0 \rightarrow ^7F_2$ to $^5D_0 \rightarrow ^7F_1$ may provide structural hints such as the distortion of CF environment and the site symmetry. The fact that $^5D_0 \rightarrow ^7F_1$ line at 594 nm (MD) is very strong in comparison to $^5D_0 \rightarrow ^7F_2$ line at 615 nm (ED) as can be seen from Figure 6b indicates that Eu^{3+} occupy (cubic) symmetric environment with inversion symmetry (O_h). But

the appearance of several weak lines in the spectra in addition to the allowed transitions for O_h symmetry indicates that other Eu^{3+} sites may be coexisting.

No emission from the host is observed, indicating the efficient energy transfer from the host group to Eu^{3+} ions.

Typical excitation spectrum monitored at 547 nm emission line of $ThO_2:Tb^3$ is depicted in Fig.8a. Excitation spectra exhibit a sharp strong band of 230 nm due to the parity- and spin-allowed transition $4f^8{\rightarrow}4f^75d^1$ of Tb [48]. The peaks in the excitation spectrum ranging from 250 to 280 nm can be clearly assigned to the spin-forbidden transition of the Tb^{3+} ions [49].

The excitation lines located around 283, 303, 317, 340, 350, 368, 377, and 486 nm are attributed to the absorption transitions from the $^7F_6$ ground state to the ^5I_J, ^5H_J, $^5D_{0,1}$, ^5G_J, $^5D_2$, $^5L_{10}$, $^5D_3$, and $^5D_4$ excited states, respectively. For finding out the origin of the PL lines, the spectrum of the ThO_2 doped with 1.0 mol% Tb is represented in Fig. 8b. The groups of intensive emission lines located at 488, 547, 585, and 620 nm are assigned to the emission transitions from the $^5D_4$ excited state to the $^7F_6$, $^7F_5$, $^7F_4$, and $^7F_3$ ground states, respectively. The emission spectra of $ThO_2:Tb^3$ show maximum intensity at 547 nm which is characteristic green emission of Tb^{3+} ions.

It is noteworthy that, along with the emission from $^5D_4$ level in systems where terbium doping levels are relatively low, the emissions which usually occur in the wavelength range of 400–450 nm, from $^5D_3$ level may be observed. In the present system, such emissions have been observed at about 418 nm ($^5D_3{\rightarrow}^7F_5$), 433 nm ($^5D_3{\rightarrow}^7F_4$) and 455 nm ($^5D_3{\rightarrow}^7F_5$). Other groups of very weak emission lines at 647, 667 and 679 nm are assigned to $^5D_4{\rightarrow}^7F_2$, $^7F_1$, and $^7F_0$ transitions, respectively (see the insets of Fig. 8b).

The green emission at 547 nm belongs to the magnetic dipole (MD) $^5D_4$-$^7F_5$ transitions of Tb^{3+}, and the transition hardly varies with the crystal field strength. The blue emission at about 488 nm ascribes to the electric dipole(ED) $^5D_4$-$^7F_6$ transitions of Eu^{3+}, which is very sensitive to the local environment around the Tb^{3+} and depends on the symmetry of the crystal field. The fact that $^5D_4{\rightarrow}^7F_5$ line at 547 nm (MD) is very strong in comparison to $^5D_4{\rightarrow}^7F_6$ line at 488 nm (ED) as can be seen from Figure 6b indicates that Eu^{3+} occupy (cubic) symmetric environment with inversion symmetry (O_h). No emission from the host is observed, indicating the efficient energy transfer from the host group to Tb^{3+} ions.

Figure 9a shows excitation spectra (λ_{em} = 572 nm) of the 1.0 mol% Dy doped ThO_2 (as prepared sample). In the excitation spectrum, a broad hump observed in the region of

220–290 nm has been attributed to the $O^{2-} \rightarrow Dy^{3+}$ charge transfer band (CTB), which is caused by the electron transfer from filled 2p orbital of O^{2-} ions to vacant 4f orbital of Dy^{3+} ions.

The sharp lines observed in the wavelength range 300-450 nm, are attributed to the 4f-4f transition of Dy^{3+}. The peaks seen at 326, 351, 366, 387, 427 and 451 nm were assigned to electronic transitions of $^6H_{15/2} \rightarrow {}^6P_{3/2}, {}^6P_{7/2}, {}^6P_{5/2}, {}^4I_{13/2}, {}^4G_{11/2}$ and $^4I_{15/2}$ respectively. Figure 9b show the emission spectra for $ThO_2:Dy^{3+}$ at 256 nm (charge transfer band) Upon excitation with 256 nm, the emission spectrum is characterized by three bands located at 482, 572 and 670 nm corresponding to the transitions $^4F_{9/2} \rightarrow {}^6H_{15/2}$ (blue), $^4F_{9/2} \rightarrow {}^6H_{13/2}$ (yellow) and $^4F_{9/2} \rightarrow {}^6H_{9/2}$ (red) respectively.

It is also known that the Dy^{3+} emission around 480 nm is of magnetic dipole and 575 nm is of electric dipole (ED) origin. Generally, when Dy^{3+} is located at a low symmetry (without an inversion center), the yellow emission is dominant, while the blue emission is stronger when Dy^{3+} is located at a high symmetry (with an inversion center). However yellow emission at 575 nm ($^4F_{9/2} \rightarrow {}^6H_{13/2}$) is predominant in Dy^{3+} ion-doped ThO_2 suggesting that the local environment around dysprosium lacks inversion symmetry. No emission from the host is observed, indicating the efficient energy transfer from the host group to Dy^{3+} ions.

3.6. Differences in local site: Luminescence life time measurement

It can be seen from the emission spectra for respective lanthanide ion; symmetric environment exists for Eu and Tb as MDT dominates over EDT whereas for Dy ion EDT dominates over MDT resulting in lower site symmetry around it in thoria. To get further insight into it lifetime measurements were carried for all three ions.

It can be seen from figure 10 and table 3 , when excited at the CTB position, biexponential behavior exists in all the cases indicating that, there are two different types of Ln3+ species in ThO_2 nanorods; short lived species ($\tau \sim 280\text{-}300$ μs, fast decaying species-S_1) and long lived species ($\tau \sim 1.4\text{-}1.7$ ms, slow decaying species-S_2). They differ only in terms of their relative population.

Usually, Ln^{3+} ions substitute Th^{4+} as a cubic site, but charge compensation often results in the presence of other centers. Doping concentration also has an important effect on the formation of the crystallographic sites. There are two kind of crystallographic sites in bulk thoria cubic (O_h) and non-cubic (C_{3v}) **[30]**. In case of nano thoria; because of smaller particle size and

higher surface –to-volume ratio, oxygen can easily be adsorbed and thus oxygen defect were formed in nanocrystalline ThO_2 during the synthesis procedure in air. These oxygen defects significantly influenced the crystal field environment of Ln^{3+}. So in nano thoria site symmetry can be further reduced that C_{3v}.

Assuming a given phonon energy (same host for the lanthanide ions), a relatively longer PL decay time should be attributed to a more symmetric site, as the f-f transition becomes more forbidden, whereas a shorter decay time is often associated with an asymmetric site due to relaxation in the selection rules. Species S_1 (270-300 µs) arises because of Ln^{3+} ions occupying non-cubic site without inversion symmetry whereas species S_2 (1.4-1.7 ms) can be ascribed to Ln^{3+} ions occupying 8-coordinated cubic Th^{4+} with inversion symmetry (Oh).

It can be inferred from all these discussion that majority of Dy^{3+} occupy only one kind of sites that arises because of charge compensation defect ($\leq C_{3v}$) whereas majority of Eu and Tb occupy 8-coordinated Th^{4+} site. Yin et al has also reported that Eu^{3+} ions have O_h and C_{3v} site symmetry in bulk ThO_2 while for Dy^{3+} only C_{3v} exists.

In fluorite structure thorium is 8-coordinated and its ionic radii is 105 pm. Since the radius difference between 8-coordinated Th^{4+} (105 pm) and 8-coordinated Dy^{3+} (102.7 pm) is larger than that between 8- coordinated Th^{4+} and 8-coordinated Eu^{3+} (106.6)/ Tb^{3+} (104 pm), most of the Dy^{3+} ions may occupy the C3v sites and partly occupy the Th^{4+} sites in $SrZrO_3$ lattice. This disturbs the local filed, where such disturbance is evidenced by the more intense emission of $^4F_{9/2} \rightarrow {}^6H_{13/2}$. It can be concluded that the DyO_8 octahedra in the thoria host lattice are distorted and there is lack of inversion symmetry at the Dy^{3+} site.

In order to identify the environment associated with the species exhibiting different life-times, time resolved emission spectra were recorded for europium doped system at different time-delays with constant integration time. After doing mathematical calculations in such a way that at longer delay shorter lived species completely decays off; spectra for short lived and long lived species obtained are shown in the Figure 11 below. As seen from the figure short lived species shows stronger emission from $^5D_0 \rightarrow {}^7F_2$ transition indicating that the Eu^{3+} ions exhibiting short life-time are in asymmetric environment without inversion symmetry. The symmetric environment observed for long lived species (1.45 ms) can be because of Eu^{3+} ions occupying Th^{4+} cubic site with inversion symmetry (O_h) and short lived species (288 µs) can be ascribed to Eu^{3+} ions occupying non-cubic site without

inversion symmetry (C_{3v}). Such site selective emission of lanthanides is known in inorganic oxides with multiple sites **[50-52]**.

3.7. Tri-doped ThO_2: Ln^{3+} (Ln^{3+}: Dy^{3+}, Tb^{3+}, Eu^{3+})

Chromaticity coordinates are one of the vital factors for evaluating performance of the prepared phosphors. Here, we investigated the luminescent color of the as-synthesized samples by using the 1931 CIE (Commission Internationale de L'Eclairage) system **[53]**. Fig. 12 presents the corresponding CIE coordinates positions, which show the different emission colors for the as-synthesized (A) ThO_2 (B) ThO_2:Eu^{3+}, (C) ThO_2:Tb^{3+} (D) ThO_2:Dy^{3+}. It can be seen that the (A) , (B) (C) and (D) samples emit blue, red–orange, green and yellowish blue and their chromaticity coordinates are mentioned in table 4.

With the aim of synthesizing white light emitting solid state phosphor, ThO_2 lattice was doped with all the three activators Tb^{3+} (green), Dy^{3+} (yellow/blue) and Eu^{3+} (red). The concentration of the lanthanide ion is 1.0 mol % Eu, 1.0 mol % Tb and 1.0 mol % Dy. The resultant emission spectra and CIE index for tri-doped doped system is shown in figure 13. Table 4 represents chromaticity coordinates for sample at different excitation wavelength. It can be seen from the table 3 that ThO_2: Ln^{3+} (Ln^{3+}: Dy^{3+}, Tb^{3+}, Eu^{3+}) shows white light emission.

The internal quantum efficiency of ThO_2: Eu^{3+} upon excitation at the maximum of the absorption bands (λ_{exc}=300 nm) were found to be 59%. These values are comparatively lower than those of the YAG: Ce (75%) **[54]** Or (Sr, Ba)$_2$SiO$_4$: Eu^{2+} (90.4%) **[55]**. Co-doping with Dy^{3+} and Tb^{3+} influences QE only slightly

Conclusions:

Reverse micellar route was employed for the synthesis of thoria nanoparticles. TEM studies shows the formation of nanorods of 2 micron length and 20 nm diameters. An undoped thoria nanorod emits blue light on UV-excitation due to presence of oxygen vacancy on the surface of nanorods. First principles calculations using PAW-PBE predicts the structural relaxations due to neutral and positively charged oxygen defects in bulk thoria leads to symmetric distortion around the vacancy site and this prediction is complemented by experimentally measured highly symmetric isotropic signal with g = 1.959 in EPR studies. Density of states analysis shows presence of defects states mainly contributed by Th d and f states near the conduction band minima for the double positively charged oxygen vacancy

and radiative transitions from these states qualitatively explains blue emission in thoria. Nanorods of thoria were found to be an excellent host for lanthanide luminescence. On doping 1.0 mol % Eu^{3+} , Tb^{3+} and Dy^{3+}, Thoria nanorods shows red , green and bluish yellow emission respectively. No host emission was found in Eu, Tb or Dy doped sample indicating completer transfer of energy. Time resolved fluorescence spectroscopy was carried to probe the life time and local structure around lanthanide ions. Broadly, two different types of lanthanide exist in thoria; long lived species (1.4-1.6 ms) and short lived species (270-300 µs). Species S_1 (270-300 µs) arises because of Ln^{3+} ions occupying non-cubic site without inversion symmetry ($\leq C_{3v}$) whereas species S_2 (1.4-1.7 ms) can be ascribed to Ln^{3+} ions occupying 8-coordinated cubic Th^{4+} with inversion symmetry (Oh). Majority of Dy^{3+} occupy only one kind of sites that arises because of charge compensation defect ($\leq C_{3v}$) whereas majority of Eu and Tb occupy 8-coordinated Th^{4+} site with inversion symmetry (Oh). Moreover, multicoloured luminescence containing white emission has been successfully achieved for tri-doped ThO_2:Ln^3 (Eu, Tb, and Dy phosphors because of the simultaneous luminescence of Ln^{3+} in the ThO_2 host. Due to their excellent emission intensity, good CIE chromaticity, superior stability and morphology uniformity, these phosphors have potential applications in field emission display devices.

References:
1. N. Kimura, K. Sakuma, S. Hirafune, K. Asano, N. Hiroski, R.J. Xie, Appl. Phys. Lett. 2007, **90**, 051109
2. E.F. Schubert, J.K. Kim, Science, 2005, **308**, 1274
3. J.R. Agger, M.W. Anderson, M.E. Pemble, O. Terasaki, Y. Nozue, J. Phys. Chem. B, 1998,**102**, 3345
4. A. Trave, F. Buda, A. Fasolino, Phys. Rev. Lett., 1996, **77**, 5405
5. J.A. Nelson, E.L. Brant, M.J. Wagner, Chem. Mater. 2003, **15**, 688
6. S. Maenosono, T. Okuba, Y. Yamaguchi, J. Nanoparticle Res, 2003, **5**, 5
7. M. P. Pileni, J. Phys. Chem. 1993, **97**, 6961
8. G. Curran, Y. Sevestre, W. Rattray, P. Allen, K.R. Czerwinski, J. Nucl. Mater. 2003, **323**, 41
9. K. Ananthasivan, S. Anthonysamy, C. Sudha, A.L.E. Terrance, P.R. Vasudeva Rao, J. Nucl. Mater. 2002, **300,** 217
10. S. Dash, A. Singh, P.K. Ajikumar, H. Subramanian, M. Rajalakshmi, A.K. Tyagi, A.K. Arora, S.V. Narasimham, B. Raj, J. Nucl. Mater. 2002, 303, 156.

11. K. Ananthasivan, S. Anthonysamy, A. Singh, P.R. Vasudeva Rao, J. Nucl. Mater. 2002, **306,** 1

12. R.D. Purohit, S. Saha, A.K. Tyagi, J. Nucl. Mater. 2001, **288**, 7

13. V.R. Choudhary, A.G. Gaikwad, S.D. Sansare, Catal. Lett.2002, **83**, 235.

14. B. Shi, H. A. Dabbagh, B.H. Davis, Top. Catal.2002, **18**, 259

15. R. Tismaneanu, B. Ray, R. Khalfin, R. Semiat, M.S. Eisen, J.Mol. Catal. A, 2001, **171**, 229

16. S.W. Ho, J. Catal.1998, **175**,139

17. F.Z. Wang, F. Zhuge, H. Zhang, B.J. Ding, Mater. Res. Bull. 2003, **38**,629.

18. F. Zhuge, Z. Ye, F. Wang, Y. Wang, H. Zhang, B. Ding, Mater. Lett.2003, **57**, 2776.

19. I.C. Cosentino, R. Muccillo, Mater. Lett.1997, **32**,295.

20. R.D. Purohit, S. Saha, A.K. Tyagi, J. Nucl. Mater. 2003,**323**,36.

21. R.S. Niranjan, M.S. Londhe, A.B. Mandale, S.R. Sankar, L.S. Prabhumirashi, K. Vijayamohanan, I.S. Mulla, Sensor Actuat. B., 2002, **87**,406.

22. S. Hubert, P. Thouvenot, J. Lumin., 1992, **54**, 103

23. S. Hubert, P. Thouvenot, J. Alloy Compd.,., 1992, **59**, 156

24. S.K. Gupta, R. Gupta, V. Natrajan, S.V. Godbole, Mater. Res. Bull., 2014, **49**, 297

25. D. Chandrasekhar, S.K. Gupta, S.V. Godbole, J. Mol. Struct.,   J. Mol. Struct., 2013, **1051**, 91

26. Z.W. Lin , Q. Kuang , W. Lian , Z. Y. Jiang , Z. X. Xie , R. B. Huang , L. S. Zheng, J. Phys. Chem. B, 2006, **110**, 23007

27. S.V. Godbole,   A.R. Dhobale,   M.D. Sastry,   Chung-Hsin Lu,   A.G. Page, J. Lumin., 2003, **105**, 89

28. S.V Godbole, J.S Nagpal, A.G Page, Radiat. Meas., 2000, **32**, 349

29. M. Yin, J.C. Krupa, Spectrosc. Spect. Anal., 2001, **21**, 418

30. M. Yin, J.C. Krupa, E.A. Fidancev, A.L. Rubben, Phys. Rev. B. , 2000, **61**, 8073

31. G. Kresse and D. Joubert, Phys. Rev. B, 1999, **59**, 1758.

32. G. Kresse and J. Furthmueller, Phys. Rev. B, 1996, **54**, 11169.

33. P. E. Blöchl, Phys. Rev. B, 1994, **50**, 17953.

34. J. P. Perdew, K. Burke and M. Ernzerhof, Phys. Rev. Lett.1996, **77**, 3865.

35. H. J. Monkhorst and J. D. Pack, Phys. Rev. B, 1976, **13**, 5188.

36. P. E. Blöchl, O. Jepsen, O. K. Andesen, Phys. Rev. B, 1994, **49**, 16223.

37. Y. Lu, Y. Yang and P. Zhang, J. Phys.: Condens. Matter, 2012, **24**, 225801.

38. I. Navas, R. Vinodkumar · V.P. Mahadevan Pillai, Appl. Phys. A, 2011,**103**,373

39. K Vanheusden, C H Seager, W L. Warren, D R Tallant, and J A Voigt, Appl. Phys. Lett.,1996, **68**, 403

40. K Vanheusden, W L Warren, C H Seager, D R Tallant, J A Voigt, and B E Gnade, J. Appl. Phys.1996, **79**, 7983.

41. A van Dijken, E A Meulenkamp, D Vanmaekelbergh, and A Meijerink, J. Phys. Chem. B, 2000, **104**, 1715.

42. K. Vanheusden, W.L. Warren, C.H. Seager, D.R. Tallant, J.A. Voigt, B.E. Gnade, J. Appl. Phys.,1996, **79**,7983.

43. P. H. Kasai, Phys. Rev.1963, **130**, 989

44. J. S. Olsen, L. Gerward, V. Kanchana, G. Vaitheeswaran, J. Alloys Compd. 2004, **381**,37.

45. E. T. Rodine and P. L. Land, Phys. Rev. B, 1971, **4**, 2701.

46. R. C. Linares, J. Opt. Soc. Am. 1996, **56**, 1700.

47. S. K. Gupta, M. Sahu, K. Krishnan, M. Saxena, V. Natarajan and S.V. Godbole, Journal of Materials Chemistry C,2013, 1, 7054

48. L. Song, P. Du, Q. Jiang, H. Cao, J. Xiong, J. Lumin. 2014, **150,** 50

49. L. Liu, R. Li, Y. Deng, L. Li, S. Lan, W. Zi, Appl. Surf. Sci., 2014, **307,** 393

50. S.K. Gupta, M. Mohapatra, S.V. Godbole, V. Natrajan, RSC. Adv. 2013, **3**, 20046

51. R. Phatak, S.K. Gupta, K. Krishnan, S.K. Sali, S.V. Godbole, A. Das, Dalton Trans., 2014, 43, 3306

52. S.K. Gupta, P.S. Ghosh, A. Arya, V. Natarajan, RSC Adv., 2014, **4**, 29202

53. N. Guo, H. You, Y. Song, M. Yang, Kai Liu, Y. Zheng, Y. Huang, H. Zhang , J. Mater. Chem., 2010, **20**, 9061.

54. A. Meijerink, W.J. Schipper, G. Blasse, J. Phys. D: Appl. Phys. 1991, **24**, 997

55. Ch.-H. Huang, T.-M. Chen, Inorg. Chem. 2011, **50**, 5725
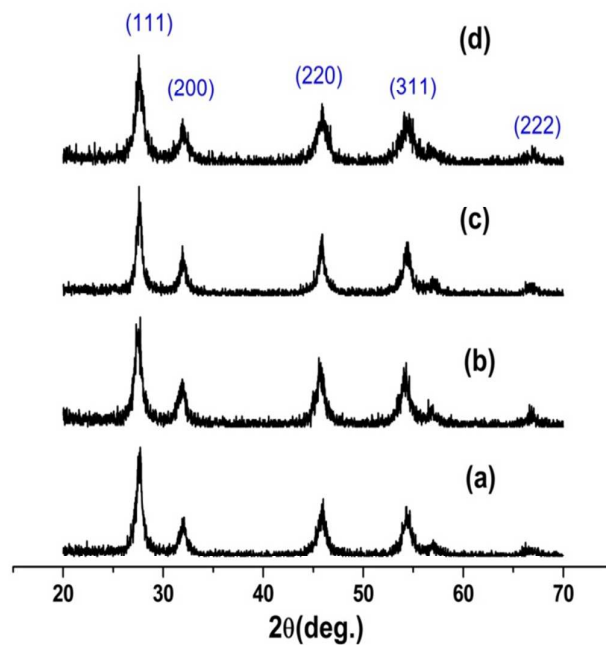
Figure 1: X-ray diffraction patterns of (a) ThO$_2$; (b) ThO$_2$: 1.0 mol% Eu^{3+}; (c) ThO$_2$: 1.0 mol% Tb^{3+} (d) ThO$_2$: 1.0 mol% Dy^{3+}
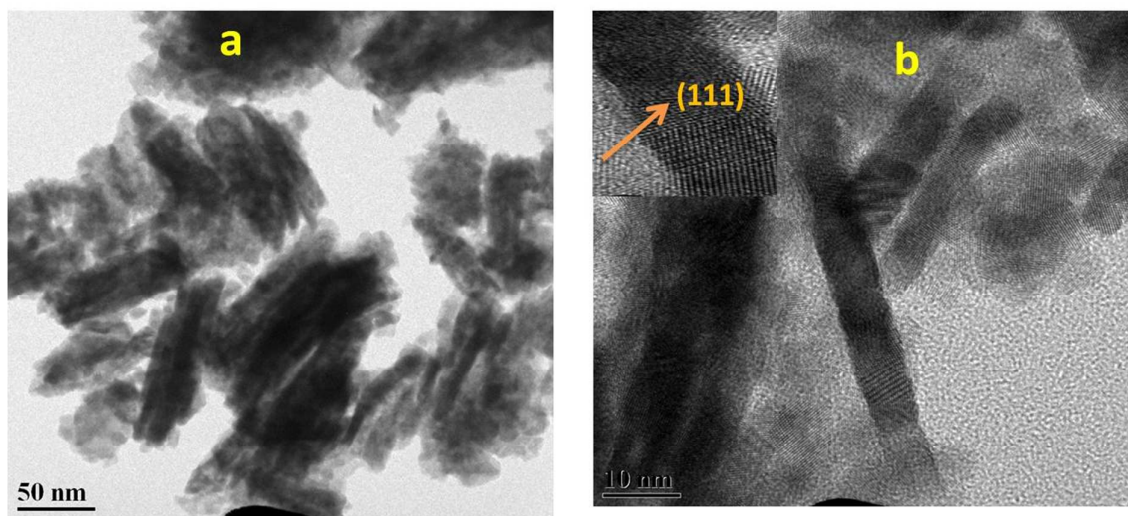
Figure 2: (a) TEM bright-field image (b) HRTEM of thoria nanocrystallites from micelle.
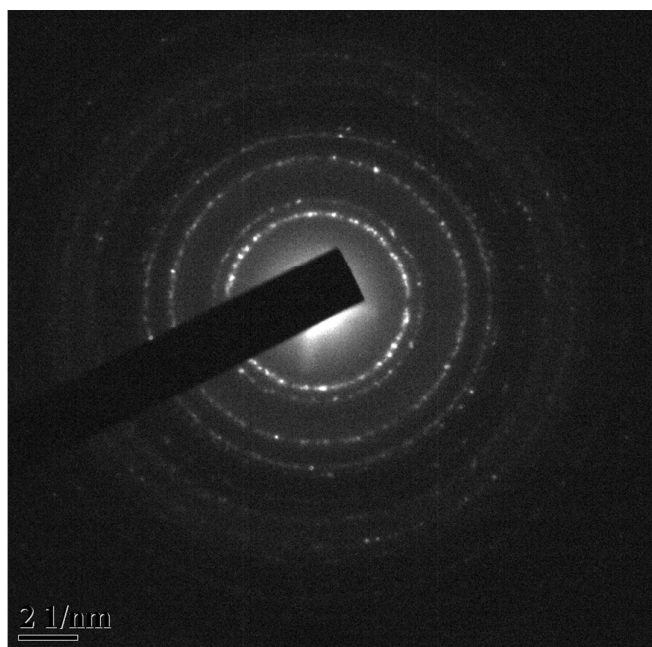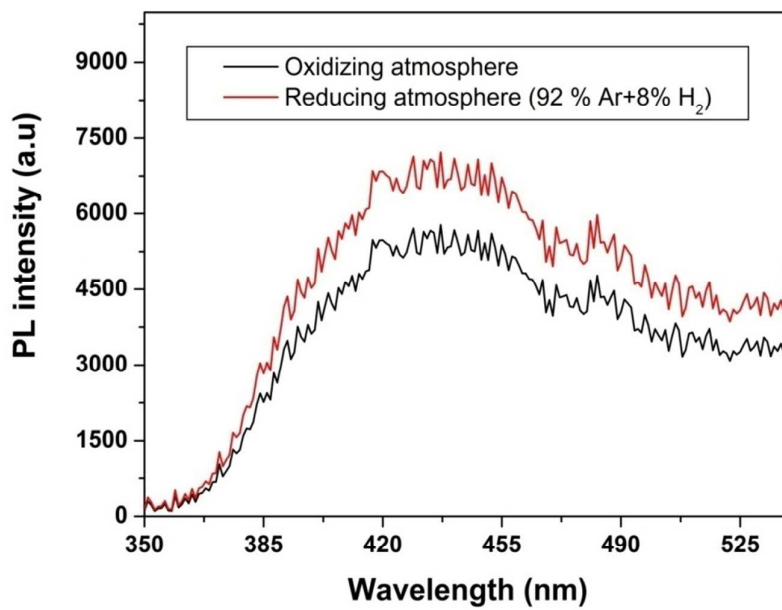
Figure 2c: SAED micrograph of thoria

Figure 3: Photoluminescence spectrum of as-prepared ThO$_2$ nanorods taken with the excitation wavelength of 248 nm.
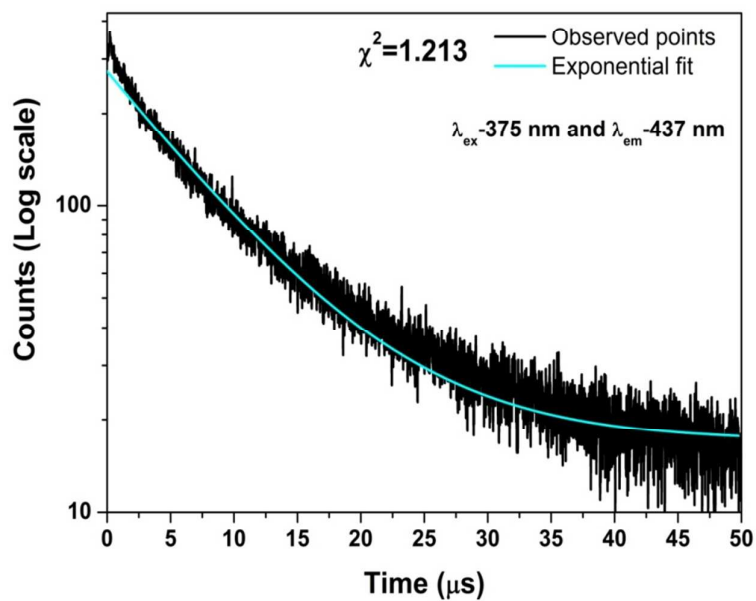
Figure 4: Decay curves for ThO$_2$ nanorods. Samples were excited at 375 nm and emission was monitored at 437 nm using pulsed diode laser.
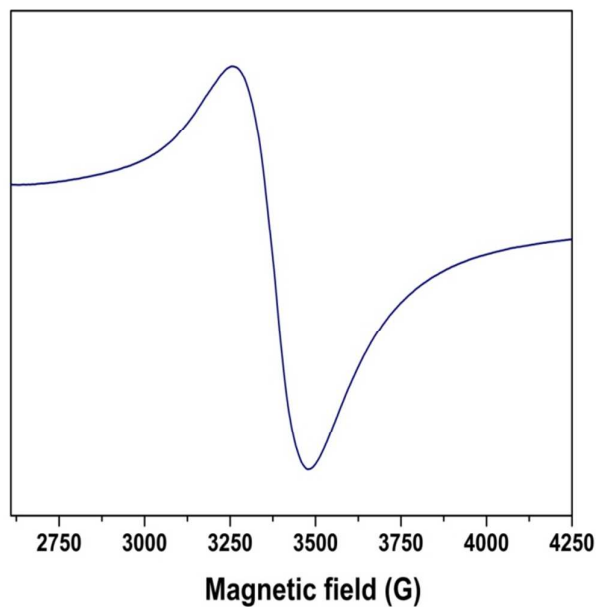
Figure 5: X-band EPR spectra thoria nanorods at room temperature
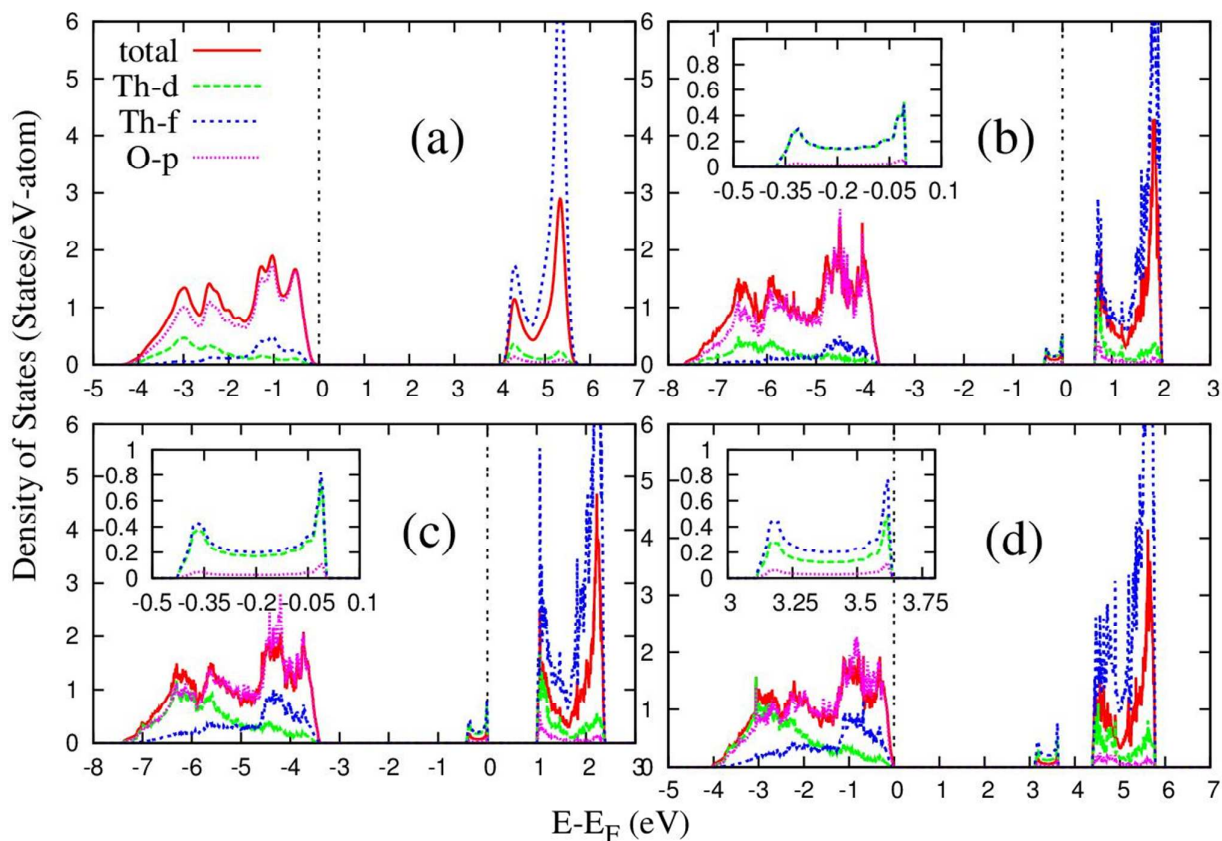
Figure 6: Total and partial DOS of (a) defect free (b) neutral oxygen defect (V_0) (c) +1 oxygen defect (V_0^{+1}) and (d) +2 oxygen defect (V_0^{+2}). Inset figure shows DOS of defect states in the forbidden energy region.
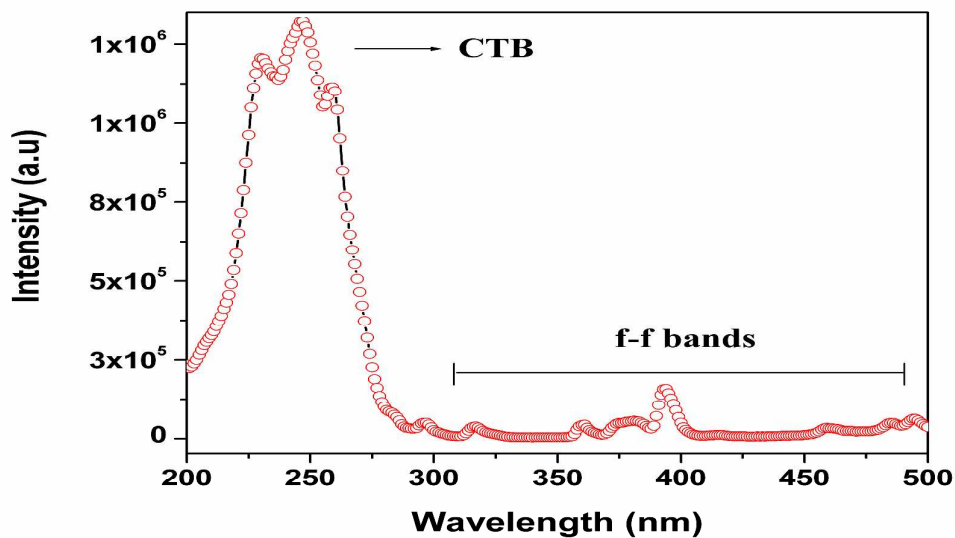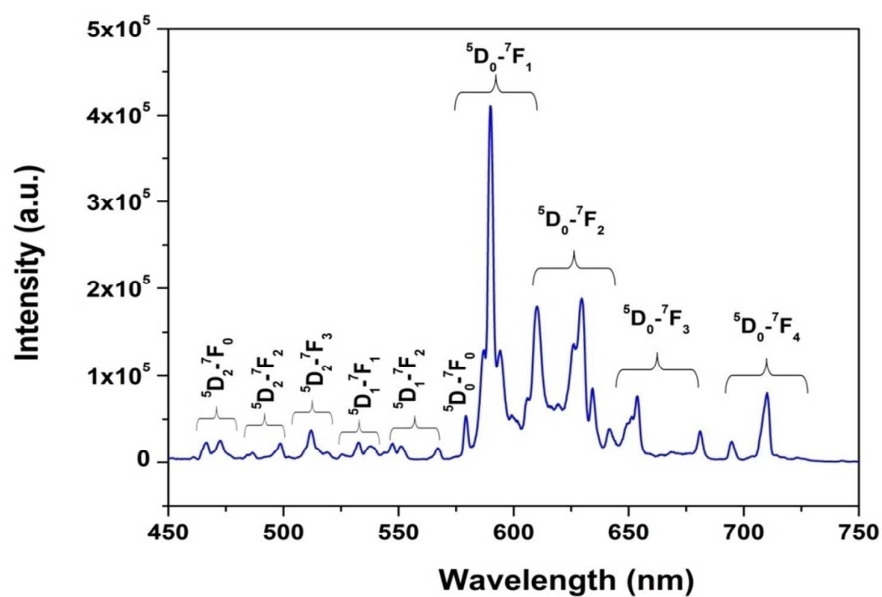
Figure 7: (a) Excitation spectra (λ_{ex}-592 nm) (b) Emission spectra (λ_{ex}-256nm) of ThO$_2$:Eu^{3+} 1.0 mol%
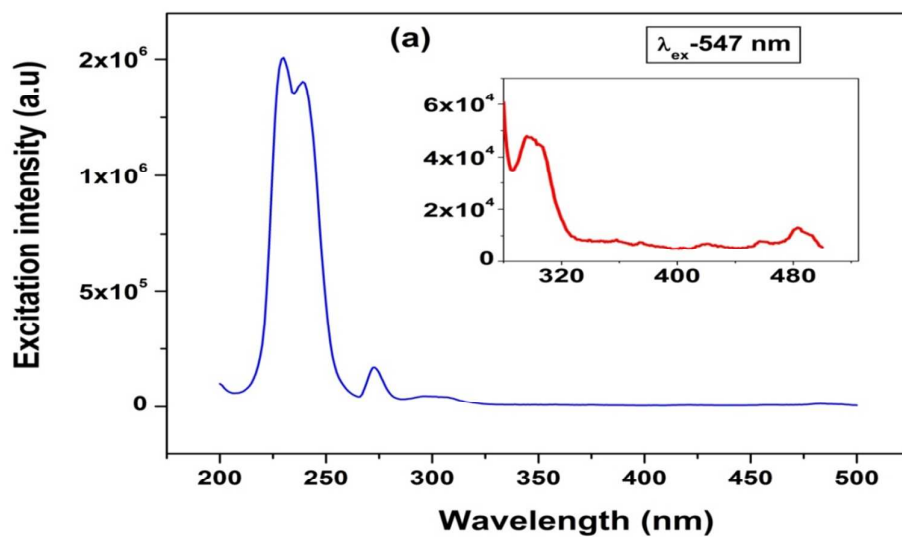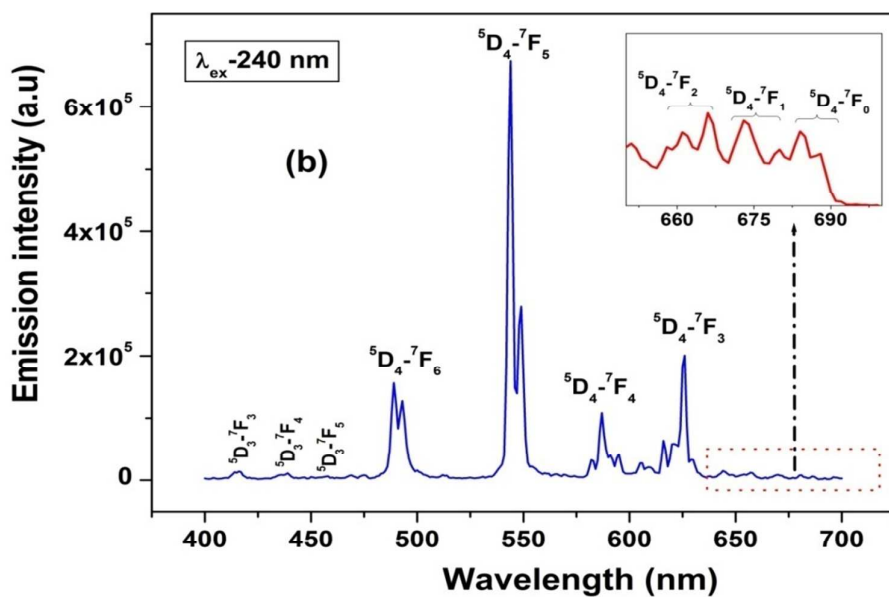
Figure 8: (a) Excitation spectra (λ_{ex}-547 nm) (b) Emission spectra (λ_{ex}-240 nm) of ThO$_2$:Tb^{3+} 1.0 mol%
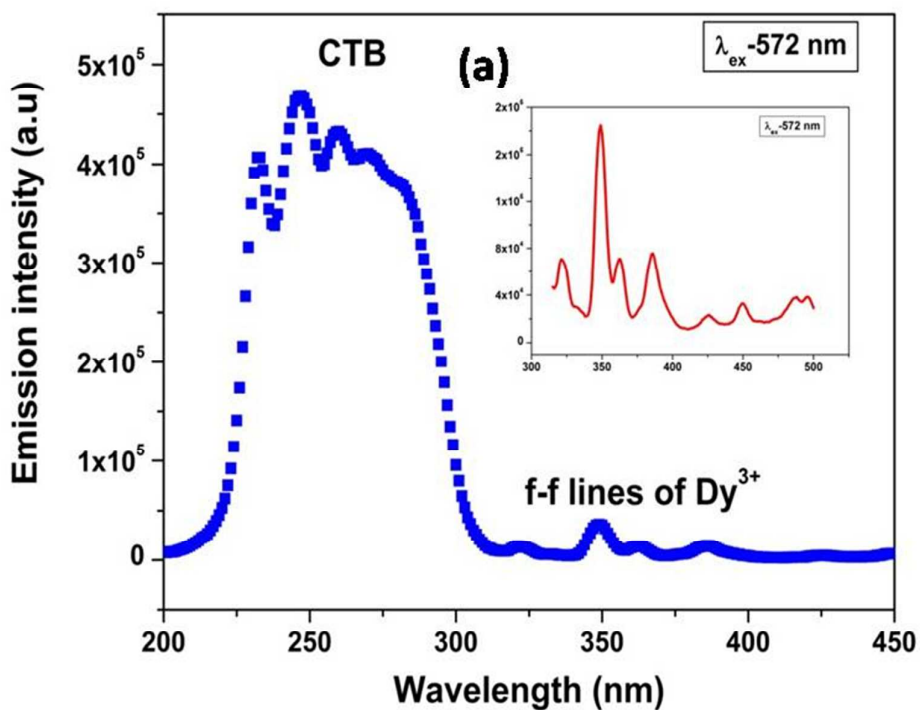
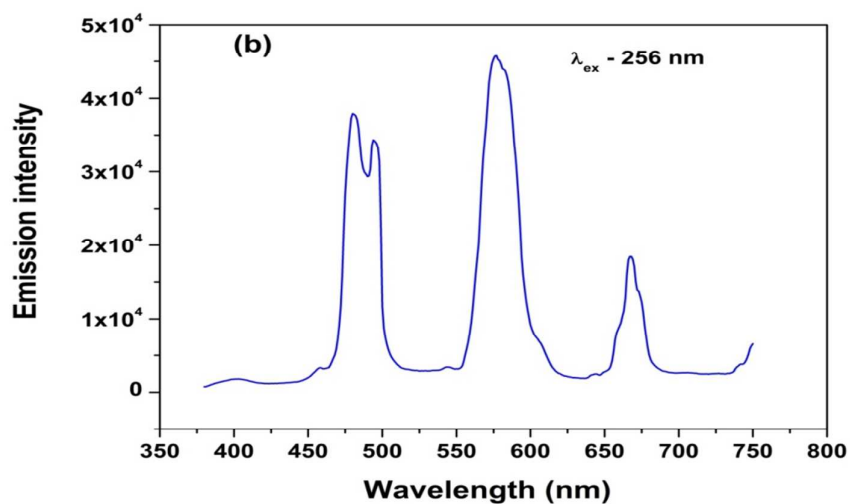**Figure 9: (a) Excitation spectra (λ_{ex}-572 nm) (b) Emission spectra (λ_{ex}-256 nm) of ThO$_2$:Dy^{3+} 1.0 mol%**

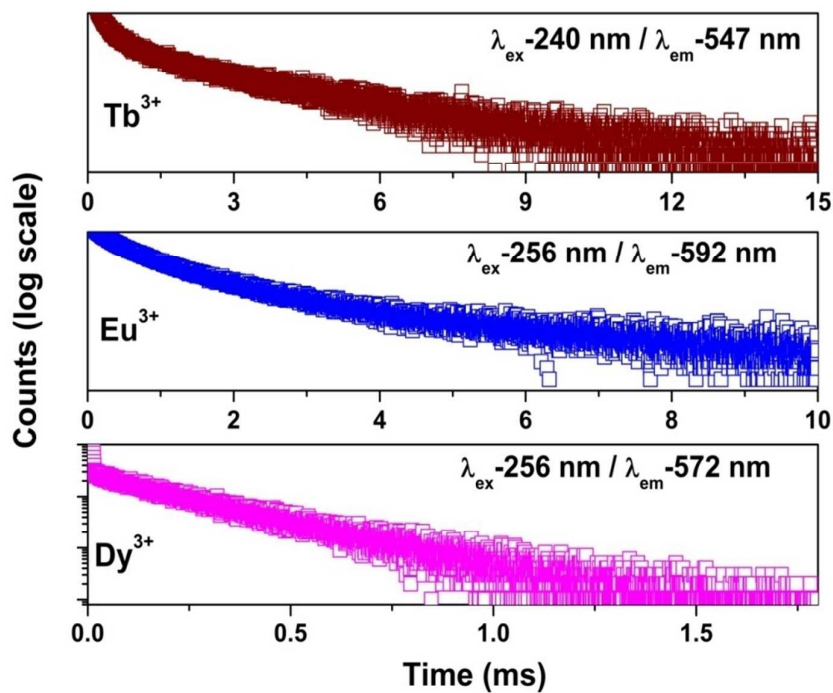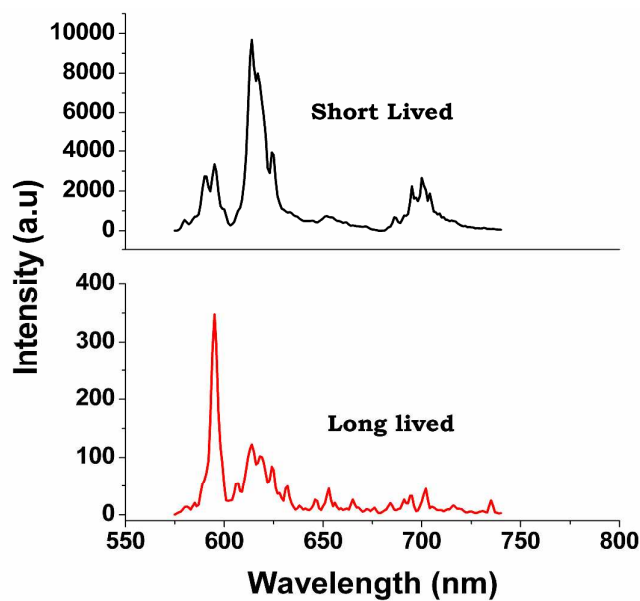**Figure 10: Decay curves for the various lanthanides in ThO$_2$**

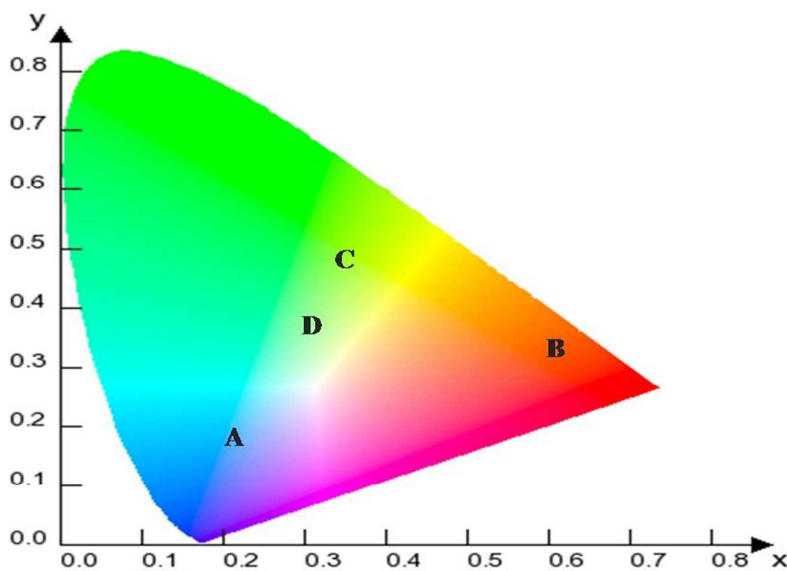**Figure 11: Time-resolved emission spectra of ThO$_2$:Eu^{3+} nanophosphor for short and long-lived species.**

Figure 12: CIE chromaticity diagram showing the emission colors for (A) ThO$_2$ (B)   ThO$_2$:Eu^{3+}, (C) ThO$_2$:Tb^{3+} (D) ThO$_2$:Dy^{3+}
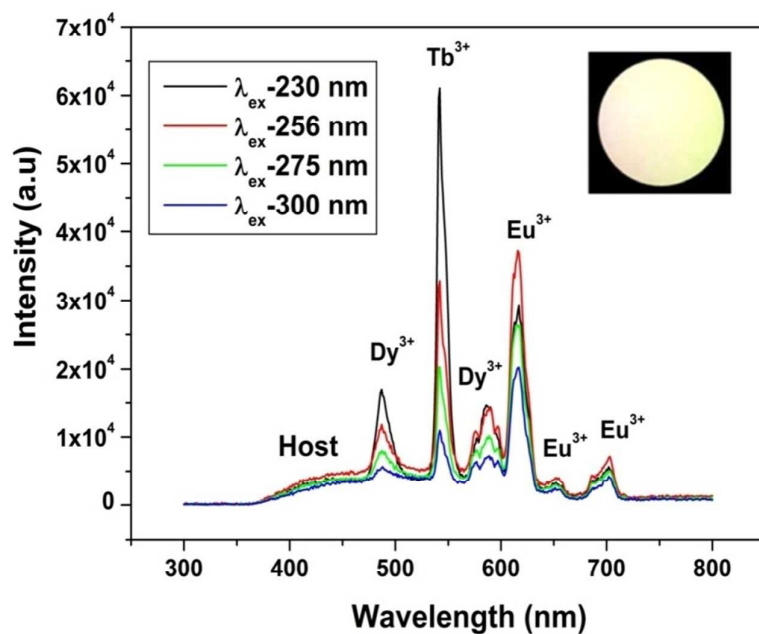
Figure 13: Photoluminescence of Eu^{3+}, Tb^{3+}, Dy^{3+} co-doped ThO_2 under different excitation. The inset shows a photograph of the obtained white light with color coordinate (0.296, 0.325).

Table 1: Trace metal assay in thoria nanorods using ICP-AES

Elements	Concentration (ppm)
Co	5.2
Cr	9.2
Cu	6.3
Fe	1.2
Mn	4.2
Ce	3.7
Dy	5.9
Eu	6.5
Gd	4.7
Sm	8.1

Table 2: Unit-cell size, distances between Th atoms in bulk ThO_2 and systems with oxygen vacancies.

Defects	Cell parameter (Å)	Distance between 1st NN (Th-Th) at defect site
Defect free	5.619	3.97
V_O^0	5.620	4.02
V_O^{+1}	5.599	4.11
V_O^{+2}	5.582	4.21

Table 3: Fluorescence decay time values for the ThO_2:Ln^{3+} (Ln= Eu, Tb, Dy) system with λ_{ex} = charge transfer band (CTB).

Ln^{3+}	Eu	Tb	Dy
τ_1 (μs)	288 (28 %)	302 (30 %)	272 (85 %)
τ_2 (ms)	1.45 (72 %)	1.65 (70 %)	1.39 (15 %)

Table 4: Chromaticity coordinates for undoped and doped thoria nanorods

Points	Products	(x, y)
A	ThO_2	(0.23, 0.19)
B	$ThO_2{:}Eu^{3+}$	(0.61, 0.32)
C	$ThO_2{:}Tb^{3+}$	(0.36, 0.49)
D	$ThO_2{:}Dy^{3+}$	(0.29, 0.37)

Table 5: Chromaticity coordinates for triply doped sample at different excitation wavelength.

λ_{ex} (nm)	X coordinate of CIE	Y coordinate of CIE
230	0.289	0.302
256	0.301	0.332
275	0.296	0.325
300	0.295	0.297